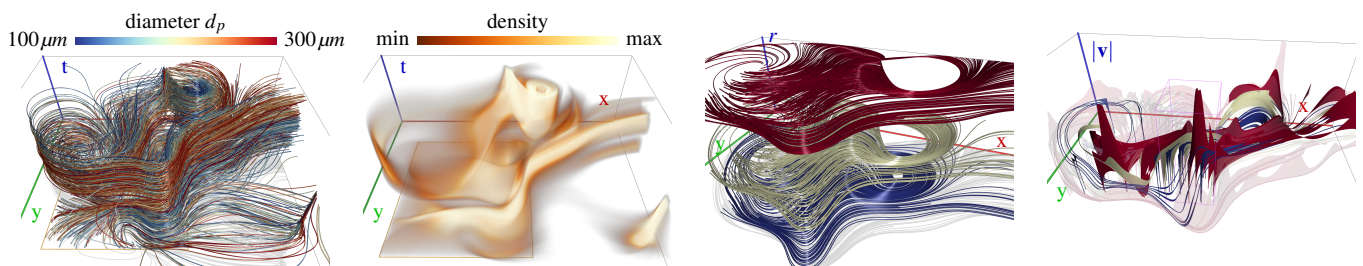


# Visualizing the Phase Space of Heterogeneous Inertial Particles in 2D Flows

Irene Baeza Rojo, Markus Gross and Tobias Günther

Computer Graphics Laboratory, ETH Zürich



**Figure 1:** Our coordinated visualizations of inertial particle motion give insights into size-dependent separation, clustering and attraction. The left image shows the individual particle trajectories of a continuous range of differently-sized particles in space-time, which can become cluttered. Thus, the second visualization displays the trajectory density, which reveals clustering regions and easier conveys an impression of the general motion. The trajectories of differently-sized particles are clearly separated in the third view. The motion of inertial particles is governed by a size-dependent attracting manifold. The last view focuses on a selection of trajectories and displays for each the distance to the attracting manifold by connecting the trajectories to the closest curve on the manifold. As shown here, heavy particles generally converge slower due to their momentum and inertia. Here, in the BORROMEAN flow with  $d_p = 100\mu m$  ( $\bullet$ ),  $d_p = 200\mu m$  ( $\circ$ ) and  $d_p = 300\mu m$  ( $\circ$ ).

## Abstract

In many scientific disciplines, the motion of finite-sized objects in fluid flows plays an important role, such as in brownout engineering, sediment transport, oceanology or meteorology. These finite-sized objects are called inertial particles and, in contrast to traditional tracer particles, their motion depends on their current position, their own particle velocity, the time and their size. Thus, the visualization of their motion becomes a high-dimensional problem that entails computational and perceptual challenges. So far, no visualization explored and visualized the particle trajectories under variation of all seeding parameters. In this paper, we propose three coordinated views that visualize the different aspects of the high-dimensional space in which the particles live. We visualize the evolution of particles over time, showing that particles travel different distances in the same time, depending on their size. The second view provides a clear illustration of the trajectories of different particle sizes and allows the user to easily identify differences due to particle size. Finally, we embed the trajectories in the space-velocity domain and visualize their distance to an attracting manifold using ribbons. In all views, we support interactive linking and brushing, and provide abstraction through density volumes that are shown by direct volume rendering and isosurface slabs. Using our method, users gain deeper insights into the dynamics of inertial particles in 2D fluids, including size-dependent separation, preferential clustering and attraction. We demonstrate the effectiveness of our method in multiple steady and unsteady 2D flows.

This is the authors preprint. The definitive version is available at <http://diglib.org/> and <http://onlinelibrary.wiley.com/>.

## 1. Introduction

Many natural physical phenomena can be described by means of vector fields, such as the motion of gases and liquids. In flow vi-

sualization, the motion of a fluid is typically assessed by the observation of massless particles, which follow the flow perfectly tangential [MLP\*10]. However, in many scientific disciplines, not

the fluid itself is of interest, but the motion of finite-sized objects immersed therein. These finite-sized objects are called *inertial particles*, which are investigated in engineering for safety concerns during helicopter take-off and landing [SGL10, SBL11, KGRK14], in automotive to estimate the soiling of cars before manufacturing [RSBE01], in biology for the dynamics of plankton transport during jellyfish feeding [PD09, SPH11], in meteorology for the study of sediment transport in desertification [SL99], or in physics for the calculation of spacecraft trajectories [SHT11]. While the motion of a massless particle is governed by a first-order ODE, the motion of a finite-sized object is described by a second-order ODE. From a physical point of view, the second-order ODE predicts both the position and velocity of an inertial particle (or position and momentum). Both combined make the analysis of particle motion a difficult high-dimensional problem, which introduces computational and perceptual challenges. For example, the current state of an inertial particle in a steady 2D flow is described as a 4D point, comprising not only a position (2D), but also a velocity (2D). The set of all possible states is called the *phase space*, which additionally depends on model-specific parameters, such as the size of the inertial particles. Visualizing the evolution of particles in the high-dimensional phase space is the key to understand, predict and compare trajectories. The trajectory of an inertial particle depends on multiple seeding parameters: the initial position, the initial velocity, and the particle size. In the recent visualization literature, the seeding parameters have always been restricted, assuming a constant initial velocity [GKKT13, GT15], homogeneous particles of the same size [GT14, GG17] or both [GT16c, GT17].

To better understand and compare inertial particle motion in steady and unsteady 2D flows, we lift this limitation. Our goal is to visualize trajectories for varying seed positions, seed velocities and heterogeneous mixtures of differently-sized inertial particles. Simply visualizing all trajectories produces significant visual clutter and thus, there are several perceptual challenges to overcome. First, the domain in which inertial particles live is high-dimensional. In previous work [GT16a, SJJ\*17], the entire space-velocity domain was visualized (for one particle size) using multi-dimensional stacking, regardless of whether particles could actually reach every location. For inertial particles in fluid flows, however, the phase space is sparsely populated [GT16c], since particles are attracted by a manifold [HS08]. Further, in many practical examples, such as in brownout during helicopter landings [SGL10, SBL11, KGRK14], inertial particles initially rest in a sediment bed, i.e., the range of initial positions and initial velocities is limited to a small subset of the domain. Both properties combined reduce the dimensionality problem considerably and pave the path towards more organized illustrations. In this paper, we propose a combination of three coordinated views that interactively visualize different aspects of the high-dimensional phase space, including the evolution over time, a clear comparison for different particle sizes and the connection to the attracting manifold. Fig. 1 gives an example: In each of the three views, we couple the 2D space with a different third dimension: time, velocity magnitude and particle size. We utilize several key concepts of visualization, such as abstraction in form of density volumes to obtain overviews, linking and brushing between the coordinated views and a highlighting of focus regions that are embedded in their surrounding context. Using our visualization tool, we gain

insights into multiple inertial fluid dynamical processes, such as the mass-dependent separation of particles, their size-dependent clustering, the attraction and size dependence of the manifold, and the interaction of particles and vortices. In all views, users can examine and compare the behaviour for different initial positions, initial velocities and different particle sizes. In summary, we contribute:

- The first interactive exploration of inertial particle trajectories that views all: varying seeding positions, seeding velocities and heterogeneous mixtures of differently-sized particles.
- Comparisons of the particle density for various particle sizes using direct volume rendering and isosurface slabs.
- Visualizations of inertial particles in space-time, as well as in the space-velocity domain in which we depict the distance to the attracting manifold using ribbons.
- A dedicated view that distinguishes the motion of discrete sets or continuous ranges of differently-sized inertial particles.

## 2. Background

This section introduces into the modeling of inertial particle motion and reviews the recent visualization work.

### 2.1. Inertial Particles

Inertial particles are finite-sized objects that are carried by fluids. Let  $\mathbf{u}(\mathbf{x}, t)$  be a two-dimensional time-dependent vector field that describes the motion of the underlying fluid, with  $\mathbf{x} \in D \subseteq \mathbb{R}^2$  and  $t \in T \subseteq \mathbb{R}$ . Next, we describe the equations of motion of inertial particles, as well as the attracting manifolds that govern their motion.

**Equations of Motion.** To this date, the Maxey-Riley equations [MR83, FH15] are considered to be the most accurate description for the motion of spherical finite-sized objects in fluids. In practice, the model is often simplified, placing several assumptions, such as that the particles are very small, the density of the particles is much higher than the density of the surrounding air and that the particles do not collide and have no effect on the fluid, cf. [SGL10, CGP\*10, PSGC11, BBC\*11, KGRK14]. Under these assumptions, the model simplifies to the following autonomous coupled first-order ODE, as described by Crowe et al. [CST98] and also cf. Günther and Theisel [GT14]:

$$\frac{d}{dt} \begin{pmatrix} \mathbf{x} \\ \mathbf{v} \\ t \end{pmatrix} = \begin{pmatrix} \mathbf{v} \\ \frac{\mathbf{u}(\mathbf{x}, t) - \mathbf{v}}{r} + \mathbf{g} \\ 1 \end{pmatrix} \quad \text{with} \quad \begin{pmatrix} \mathbf{x} \\ \mathbf{v} \\ t \end{pmatrix} (0) = \begin{pmatrix} \mathbf{x}_0 \\ \mathbf{v}_0 \\ t_0 \end{pmatrix} \quad (1)$$

where  $\mathbf{x}_0$ ,  $\mathbf{v}_0$  and  $t_0$  are seed position, seed velocity and seed time. In dynamical systems, the space of all particle states  $(\mathbf{x}, \mathbf{v}, t)$  is called the *phase space*. The time-dependent path of inertial particles is described by tangent curves of Eq. (1). Parameter  $r$  is the particle *response time*, which depends on particle diameter  $d_p$ , particle density  $\rho_p$  and the viscosity of the surrounding air  $\mu$ :

$$r = \frac{d_p^2 \rho_p}{18 \mu} \quad (2)$$

Throughout all experiments, we set as particle density  $\rho_p$  the density of dry sand, i.e.,  $\rho_p = 1600 \text{ kg/m}^3$ . The diameter  $d_p$  was set between  $40 \mu\text{m}$  and  $500 \mu\text{m}$  and the surrounding medium was assumed to be

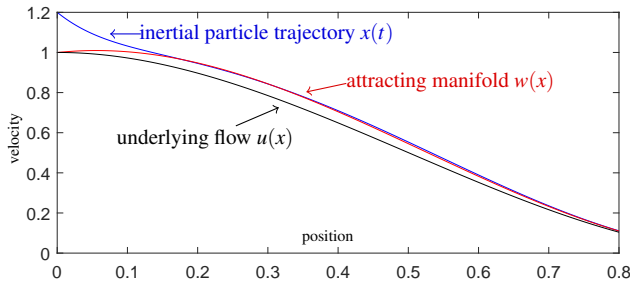


**Figure 2:** Convergence of an *inertial particle* with  $d_p = 100 \mu\text{m}$ , and seed  $(x_0, v_0) = (0, 1.2)$  toward the attracting *manifold* in the space-velocity plot. The underlying flow  $u(x) = 1 - 3x^2 + 2x^3$  is shown in black. Note the shallow extremum of the manifold at 0.054.

air. Thus, the viscosity was set to  $\mu = 1.532 \times 10^{-5} \text{ kg}/(\text{m} \cdot \text{s})$ . If not mentioned otherwise, a gravity-free environment is assumed, i.e.,  $\mathbf{g} = (0, 0)^T$ . Since particle density  $\rho_p$  and air viscosity  $\mu$  are constant, we interchangeably use response time  $r$  or particle size  $d_p$  to describe the mass dependence. For simplicity, we refer to inertial particles as light or heavy, which is common in the literature [BBC\*11, SBR16].

**Attracting Manifold.** The velocity term  $\frac{dv}{dt}$  of Eq. (1) shows that depending on response time  $r$  and gravity  $\mathbf{g}$ , particles strive to align their own velocity  $\mathbf{v}$  with the underlying flow  $\mathbf{u}(\mathbf{x}, t)$ . This gives rise to an asymptotic behaviour that is unique for inertial particles in fluids and is not generally found in other second-order ODEs, such as gravitational systems [SBHH15, SJJ\*17] or general dynamical systems [WLG97]. Thus, for inertial particles, each point  $(\mathbf{x}, t)$  in space and time is associated with a fluid velocity  $\mathbf{u}(\mathbf{x}, t)$  and an asymptotic inertial particle velocity  $\mathbf{w}(\mathbf{x}, t)$ . In the phase space of the inertial particle motion, the asymptotic inertial particle velocity forms a slowly attracting manifold, cf. Haller and Sapsis [HS08]:

$$M_r = \{(\mathbf{x}, \mathbf{v}, t) : \mathbf{w}(\mathbf{x}, t), (\mathbf{x}, t) \in D \times T\} \quad (3)$$

A first-order approximation of the asymptotic velocity of inertial particles on the attracting manifold is:

$$\mathbf{w}(\mathbf{x}, t) = \mathbf{u}(\mathbf{x}, t) + r \left[ \mathbf{g} - \frac{D\mathbf{u}(\mathbf{x}, t)}{Dt} \right] \quad (4)$$

A derivation is given in Appendix A. Eq. (4) shows that the manifold depends on the response time  $r$ , and that for massless particles the asymptotic velocity approaches the underlying flow, i.e.,  $\lim_{r \rightarrow 0} \mathbf{w}(\mathbf{x}, t) = \mathbf{u}(\mathbf{x}, t)$ . To this date, the interaction of inertial particles with the manifold has not been visualized for ranges of different response times. A part of our visualizations is dedicated to this aspect of the phase space. To illustrate the concept of slowly attracting manifolds, Fig. 2 gives a 1D example for a single inertial particle.

## 2.2. Related Work in Visualization

The trajectory of an inertial particle depends on its initial parameters, i.e., seed location, seed velocity, seed time and the particle size itself. In the following, we briefly review the visualization work and discuss the initial parameter variations that were studied.

Roettger et al. [RSBE01] visualized particle distributions on car surfaces to estimate their soiling. Günther et al. [GKKT13] extracted integral curves of inertial particles, which visualize the outcome

when varying one initial parameter, with the others remaining constant. Günther et al. extracted local information, including vortex corelines [GT14] and critical points in steady flows [GT16a, GG17], which only depend on the particle size. These structures have been extracted everywhere in the domain, regardless of whether particles can reach the locations. Stable sets were shown by Günther and Theisel [GT16a] with multi-dimensional stacking for variations of both the initial position and the initial velocity. However, the particle size was assumed to be constant throughout the domain. For inertial particles in unsteady flow, separation is frequently studied with the finite-time Lyapunov exponent [Sha05, HY00], which measures the separation due to a small perturbation of the seed position [PD09, SH09]. Garaboa-Paz and Pérez-Muñuzuri [GPPMn15] studied separation in the full phase space, and Sagristà et al. [SJJ\*17] viewed the separation in the position and velocity subspace using multi-dimensional stacking. They studied n-body problems and did not observe the influence of the variation of the particle size, which was studied by Günther and Theisel [GT15], keeping the seed velocity constant. The backward integration of inertial particles is challenging, since the attraction to the aforementioned manifold during forward integration leads to a repelling nature during backward integration, which amplifies numerical errors exponentially. Günther and Theisel [GT16c, GT16b] proposed alternative methods for backward integration, which they used to compute attracting structures [GT17]. In their experiments, the initial velocity and the particle size were kept constant. Günther and Theisel [GT16c] found that the phase space of inertial particles is sparsely populated. For a constant initial velocity, they visualized for discrete points in the domain all velocities with which inertial particles pass by, showing that velocities assemble curves. In this paper, we utilize the sparsity and aim to visualize the particle trajectories in the phase space.

None of the above papers visualized the influence of seed positions, seed velocities, seed time and the particle size together. Most previous work only depicted trajectories in the space-time domain, except for the multi-dimensional stacking [GT16a, SJJ\*17]. An early illustration of the space-velocity domain for single particles was shown by Haller and Sapsis [HS08]. In this paper, we extend the space-velocity domain and visualize the interaction with the attracting manifold. Additionally, we propose a coordinated space-response view to clearly separate size-dependent effects.

## 3. Heterogeneous Inertial Particles in Phase Space

Inertial particle motion is high-dimensional, comprising position, velocity, time and particle size. To deal with this complexity, we propose to combine multiple coordinated views that illuminate different aspects of the various dimensions. Next, we set the goals for the visualization, provide a general overview and afterwards elaborate on the individual views and the user interaction in more detail.

### 3.1. Goals

To obtain an effective visualization of inertial particle trajectories in both steady and unsteady 2D flows, the visualization system should:

- **Seeding (G1).** Compare inertial particle trajectories for ranges of seed positions, seed velocities and varying response time. Visualize heterogeneous mixtures of inertial particles using either

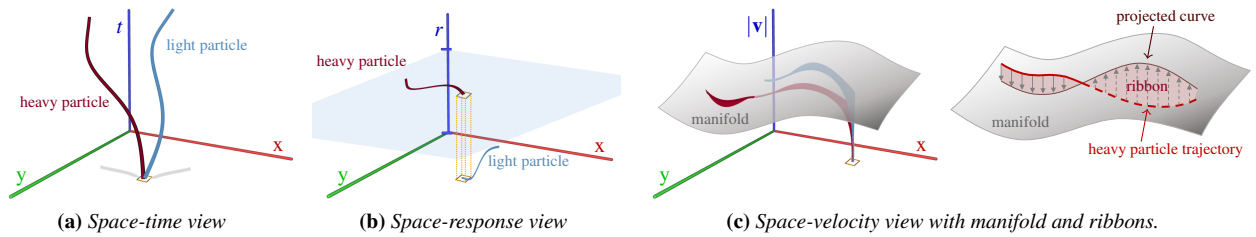


**Figure 3:** Schematic illustrations of our three coordinated views. Each view maps one aspect of the inertial phase space into a 3D subspace.

a discrete number of particle sizes (which mimics experimental setups), or a continuous spectrum of varying particle sizes.

- **Temporal Evolution (G2).** Compare the temporal evolution of inertial particle trajectories and visualize how far differently-sized particles travel in the same amount of time.
- **Particle Size (G3).** Effectively visualize and compare the differences in particle trajectories among differently-sized particles. Very often, the trajectories intersect in space, which makes the differences difficult to see. Thus, a comparative visualization needs to be designed that specifically supports this task.
- **Phase Space (G4).** Visualize inertial particle trajectories in the high-dimensional space-velocity domain in which the particles live, i.e., the phase space. Further, visualize the interaction of inertial particles with the slow attracting manifold in phase space. Show for various particle sizes how and where the trajectories cross the manifold and how far they are away from it.
- **Interactivity (G5).** Allow for an interactive exploration of the seeding parameters, as well as the visualization parameters. Interactivity is crucial in exploratory visualizations. Especially here, since the space of seeding configurations is large.

To achieve these goals, we develop an interactive visualization tool that consists of three coordinated views, each of them specifically tailored to fulfill certain aspects of our goals. In the design of the visualization, we follow common visualization patterns: overview & detail, focus & context, as well as linking & brushing [Kei02].

### 3.2. Overview

Fig. 3 gives a schematic overview of our three coordinated views. In the following, we briefly summarize them and afterwards elaborate on their design in Sections 3.3–3.5.

**Space-Time View.** The *space-time view* in Fig. 3a compares the evolution of particles over time by mapping the time to the third dimension. In this view, users can compare the trajectories of particles for different ranges of initial positions, initial velocities and particle sizes (G1), observe their temporal evolution (G2) and interactively navigate and explore the seeding parameters (G5).

**Space-Response View.** Since inertial particle trajectories intersect in space-time, the comparison of differently-sized particles can be significantly hindered due to occlusion. The *space-response view* in Fig. 3b separates the trajectories of inertial particles by their size by mapping the particle response time to the third dimension. For varying seeding configurations (G1), the size-dependent behaviour of inertial particles (G3) can be explored interactively (G5).

**Space-Velocity View.** Finally, we use the *space-velocity view* in Fig. 3c, which maps the particle’s velocity magnitude onto the third dimension. This view visualizes the interaction of inertial particles with their corresponding size-dependent attracting manifold. For this, we draw ribbons that connect the trajectory itself with its projection onto the manifold, which provides deeper insights into the attraction and interaction with the manifold in the phase space, including manifold intersections and the convergence rate. The seeding configurations can be explored (G1) and the motion in the space-velocity domain (G4) is visualized interactively (G5).

### 3.3. Space-Time View

Our first view visualizes the inertial particle trajectories in space-time. Formally, this view maps the position  $\mathbf{x} \in D \subseteq \mathbb{R}^2$  and time  $t \in T \subseteq \mathbb{R}$  of each inertial particle into a 3D domain, using:

$$f : D \times T \rightarrow \mathbb{R}^3, \text{ with } f(\mathbf{x}, t) = \begin{pmatrix} \mathbf{x} \\ t \end{pmatrix} \quad (5)$$

**Trajectory Plot.** As detail view, Fig. 4a shows the trajectories of inertial particles that were seeded from a single seed position with varying initial velocity. While in this example two discrete particle sizes have been used, we also support the display of continuous ranges of particle sizes, as shown in Fig. 1a. Same as in all remaining views, the colour of the trajectories encodes the particle size. The lines are shaded with illuminated streamline shading [ZSH96] and drop shadows are added to improve the depth perception. To emphasize the temporal evolution and to encode the flow direction, we animate the trajectories over time by adjusting the line width through a sawtooth wave. Alternatively, transparency may be used, though this would require an order-dependent image compositing. While the direct plotting of trajectories provides a detailed view onto the individual particle behaviour, plotting all trajectories directly may result in dense line sets that exhibit a significant amount of occlusion, which could be reduced by opacity optimization [GTG17].

**Density Plot.** To obtain an overview of the flow and to encode the line density, we progressively voxelize trajectories into a density volume, as shown in Fig. 4b, using direct volume rendering. The volumes are either constructed for a discrete number of particle sizes or for a continuous range as in Fig. 1b, which is encoded by an interactively adjusted transfer function. For one particle size, we color-code the density and for multiple particle sizes, we color-code the particle size. The density volume computation is similar to Ferstl et al. [FBW16], but is deferred over multiple frames to obtain fast interactive feedback. The progressive computation and the volume rendering are detailed in Section 4. In addition to direct volume

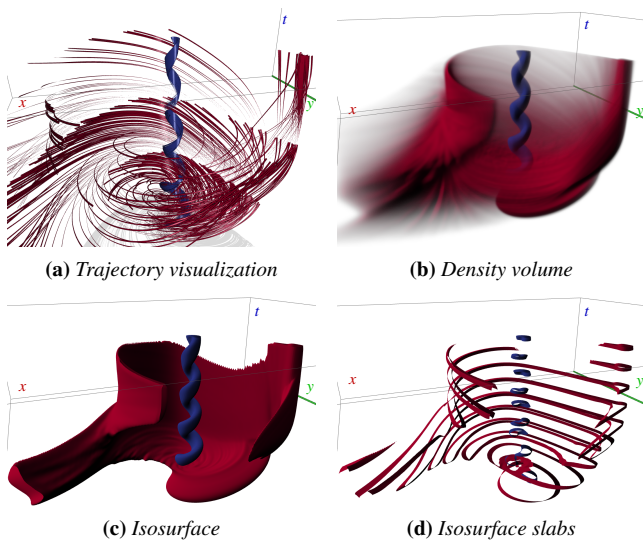


**Figure 4:** The four components of the space-time view, here shown for the BORROMEAN data set for two particle sizes  $d_p = 100\mu\text{m}$  (●) and  $d_p = 300\mu\text{m}$  (●), and a range of initial velocities.

rendering, we use isosurfaces, shown in Fig. 4c. Since isosurfaces of different particle sizes may be nested and therefore occluded, we alternatively display equidistant isosurface slabs, see Fig. 4d.

The trajectory plots and the density plots are available in all coordinated views, as they provide a detail & overview mechanism.

### 3.4. Space-Response View

In the previous *space-time* view, trajectories of different particle sizes may intersect and overlap, which can hinder the study of size-dependent differences. To address this issue, we provide a *space-response* view, which is dedicated to the comparison of possibly many differently-sized particles. The view is given by a mapping of particle position  $\mathbf{x} \in D \subseteq \mathbb{R}^2$  and response time  $r \in R \subseteq \mathbb{R}$  as:

$$g : D \times R \rightarrow \mathbb{R}^3, \text{ with } g(\mathbf{x}, r) = \begin{pmatrix} \mathbf{x} \\ r \end{pmatrix} \quad (6)$$

where the response time domain  $R$  is spanned by the minimum diameter  $d_{min}$  and maximum diameter  $d_{max}$  using the relationship in Eq. (2). The user can choose to visualize a continuous or discrete range of particle sizes, as well as abstractions of the trajectories in form of density plots or a detailed view with individual trajectories.

Fig. 5 displays the *space-response* view for the seeding configurations, used in Fig. 4. In Fig. 5a, a continuous range of differently-sized inertial particles is displayed, and in Fig. 5b the differences of two discrete particle sizes are shown. Since the size of inertial particles remains constant over time, the particles move horizontally.

### 3.5. Space-Velocity View

The *space-velocity* view explores the relationship between particle position and velocity. Formally, the view is obtained by a map from particle position  $\mathbf{x} \in D \subseteq \mathbb{R}^2$  and particle velocity  $\mathbf{v} \in V \subseteq \mathbb{R}^2$  to a

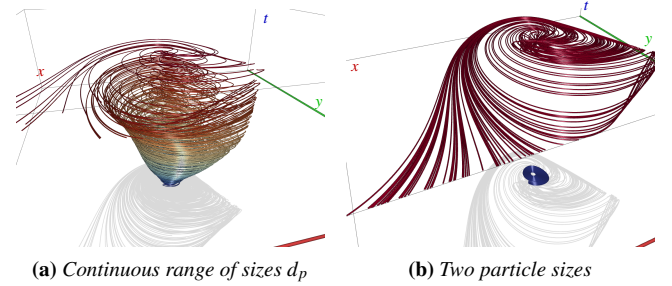


**Figure 5:** Space-response view of the BORROMEAN data set. Left: continuous heterogeneous mixture of inertial particles. Right:  $d_p = 100\mu\text{m}$  (●) and  $d_p = 300\mu\text{m}$  (●).

3D space, using the velocity magnitude as the third dimension:

$$h : D \times V \rightarrow \mathbb{R}^3, \text{ with } h(\mathbf{x}, \mathbf{v}) = \begin{pmatrix} \mathbf{x} \\ |\mathbf{v}| \end{pmatrix} \quad (7)$$

where  $|\mathbf{v}| = \sqrt{\mathbf{v}^T \mathbf{v}}$  denotes the  $L_2$  norm of a vector.

**Manifold.** In Section 2, we determined that the motion of finite-sized objects is heavily influenced by an attracting manifold in phase space, cf. Eqs. (3) and (4). The strong attraction leads the particles onto a manifold with velocity magnitude  $|\mathbf{w}(\mathbf{x}, t)|$ , cf. (4), and thus towards less visual clutter. Since the attracting manifold is size-dependent, the visualization of a range of differently-sized particles entails several different manifold surfaces that intersect with each other. For clarity, we visualize the manifold of only one interactively specified particle size with a transparent surface for one time step. In Figs. 6a and 6b inertial particle trajectories and their manifold are shown for two different particle sizes. These views give an overview of the manifolds and it becomes apparent that trajectories dive up and down, oscillating around their manifold. However, comparing distances to the manifold among multiple trajectories remains a difficult task, especially for differently-sized particles.

**Ribbons.** To compare the interaction of differently-sized inertial particles with their attracting manifold, we introduce an alternative visualization. Projecting a particle trajectory onto its corresponding manifold gives an offset curve. Triangulating the space between the trajectory and its offset curve results in a ribbon that efficiently encodes the distance to the manifold through the surface area. Since each particle trajectory is projected onto its own manifold, heterogeneous mixtures of inertial particles can easily be shown together. Moreover, in unsteady flows, particles are projected using their current time, enabling the time-dependent exploration of the manifolds. Fig. 6c gives an example of the ribbon visualization for two different particle sizes. It is directly apparent that lighter particles are attracted by the manifold faster and generally stay closer to it, as visible by the difference in ribbon surface area. Heavier particles on the other hand frequently oscillate around the manifold, never reaching the manifold in places where its velocity changes quickly. The density volume in Fig. 6d reveals the main pathways of the inertial particles.

### 3.6. User Interaction

**Seeding.** An essential aspect of the exploration is the modification of seeding parameters. In our visualizations, users can interactively

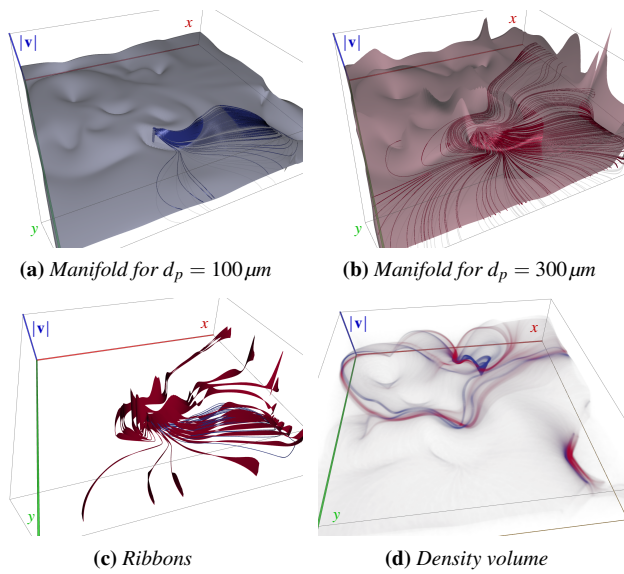


**Figure 6:** Space-velocity view of BORROMEAN data set for  $d_p = 100\mu\text{m}$  ( $\bullet$ ) and  $d_p = 300\mu\text{m}$  ( $\bullet$ ). First row, trajectories with their manifold. Second row, ribbons and density volume for both sizes.

adjust the seed box, which is specified by ranges of initial positions, initial velocities, a time range and a particle size range that are all uniformly sampled. Other distributions that mimic real-world scenarios in terms of sand grain distributions are imaginable as well. The seed box is displayed in all views in orange, see for example Fig. 3. By the specification of the seeding parameters, it is possible to seed from a single point with a range of initial velocities and vice versa, or with ranges of both initial position and velocity.

To specify the initial velocity, we use a *velocity disc*, which is illustrated in Fig. 7. The velocity range is specified by a magnitude range  $[v_{min}, v_{max}]$  and an angle range  $[\alpha_{min}, \alpha_{max}]$ , which can be areas or single points in the disc. The maximum initial velocity magnitude is user-specified and is located at the border of the disc. The selected range is highlighted in orange. If not mentioned otherwise, we set  $v_{min} = 0$ ,  $v_{max} = 1$ ,  $\alpha_{min} = 0$  and  $\alpha_{max} = 2\pi$ .

**Focus & Context and Linking & Brushing.** In order to focus on specific parameter configurations without losing context of the flow in the rest of the domain, it is possible to select certain ranges of positions, velocities and sizes that are highlighted in the visualization. The focus range is displayed with a magenta box. Fig. 8 shows

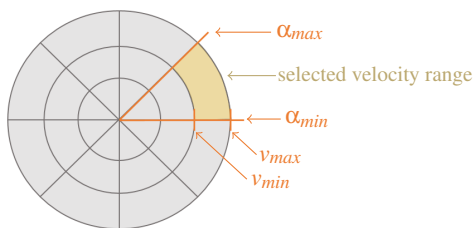


**Figure 7:** Illustration of the velocity disc, which is used to select the range of initial velocities in polar coordinates. The magnitude range is given by  $[v_{min}, v_{max}]$  and the angle range by  $[\alpha_{min}, \alpha_{max}]$ .

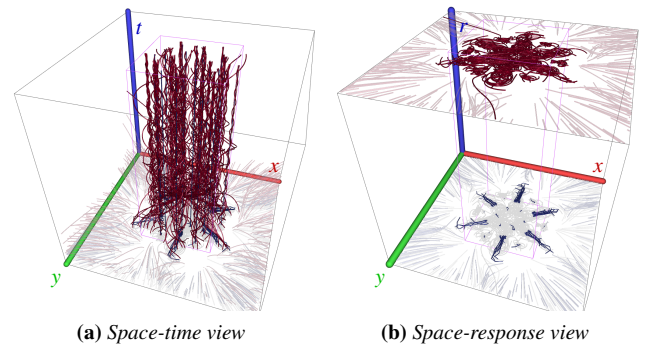


**Figure 8:** Two coordinated views on the BENZENE data set. In the center of the domain (magenta box), a focus region is applied, while the remaining trajectories are shown semi-transparently as context.

an example of a *space-time* and a *response-time* view where only a portion of the space is selected as focus of study, while the context is displayed semi-transparently. Selections that are made in one view are carried out in the other coordinated views as well, which allows linking and brushing across all views.

#### 4. Implementation

We calculated inertial particle trajectories by solving Eq. (1) with a fourth-order Runge-Kutta integrator with fixed step size [PTVF96]. The trajectories are stored in two buffers: one for the trajectory views (static) and one that is used to compute the density volumes.

**Density Volumes.** To compute density volumes, we extend the method of Ferstl et al. [FBW16], who voxelized the vertices of a fixed number of trajectories into a volume, using a certain smoothing kernel. Since some of our paths have a low probability to be sampled, we use Monte Carlo sampling to consider the full seeding space and similarly rasterize the vertices of trajectories into a 3D texture with one, two or four 32-bit float components, depending on the number of particle sizes that are displayed. Thus, each frame the progressive buffer is filled with new trajectories. By multiplying only the first integration step size with a uniform random number in  $[0, 1]$  (while keeping all remaining steps constant), the vertices uniformly sample the full integration duration, which leads to an unbiased sampling of the complete trajectories. Distance computations between voxels and line segments are therefore not necessary. To obtain a smooth early solution, we similarly employ a smoothing kernel, which introduces bias. In the spirit of progressive photon mapping [HJ09], the bias would vanish if the smoothing kernel would shrink over time.

**Volume Rendering.** We employ ray marching with early ray termination for the direct volume rendering and estimate gradients for shading using central differences. The isosurfaces are computed by ray marching and are refined by a binary search. For an introduction to volume rendering, we refer to Hadwiger et al. [HLSR09].

**Transparency.** We render semi-transparent surfaces using sub-sampling screen-door transparency [MGvW98]. This order-independent method approximates transparency by masking out selected sub-samples during the  $4\times$  multi-sampling to display the manifold and the ribbons at reduced opacity, i.e., subpixel coverage.

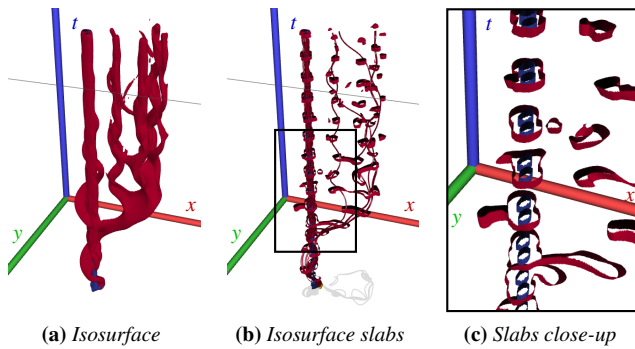


**Figure 9:** Space-time views on the BENZENE data set for  $d_p = 100\mu\text{m}$  (●) and  $d_p = 500\mu\text{m}$  (●). The isosurface slabs provide a better view on the inner nested surfaces.

## 5. Results

In this section, we apply our method to both steady and unsteady 2D flows and show how the proposed coordinated views provide a deeper understanding of the inertial particle motion. The steady flows are purely synthetic examples that exhibit complex inertial particle dynamics. Such theoretical studies are not uncommon in the fluid literature on inertial particles [HS08, SBR16]. Our unsteady fluid flows, however, resemble practical scenarios and allow for a direct interpretation of the fluid dynamical processes.

### 5.1. Steady Flows

**Benzene Molecule.** We used the central 2D slice projection of the BENZENE data set of Zöckler et al. [ZSH96], which contains an analytic approximation of a 3D magnetic vector potential of a benzene molecule. Fig. 8 shows the trajectories in the *space-time* and *space-response* view for zero initial velocity and two particle sizes. The first view shows the strong attracting critical points in the center of the domain, which attract light and heavy particles alike. While light particles have a direct and short path towards them (see lower slice Fig. 8b), heavy particles show oscillation around the critical points. The *space-response* view provides an unhindered view on the differences among the trajectories for these two particle sizes. The oscillation of heavy particles is apparent by the longer trajectories. Fig. 9a shows isosurfaces of the trajectory density volumes. The nested isosurfaces of light particles become visible with the isosurface slabs in Figs. 9b and 9c.

**Borromean Rings.** The BORROMEAN data set was kindly provided by Candelaresi and Brandenburg [CB11] and contains a simulation of the topological reconnection of two magnetic rings that initially rest in the shape of interlocked Borromean rings that decay over time. Similar to Günther and Theisel [GT16a], we selected a slice that contains swirling and non-swirling fixed points. As already shown in Figs. 4, 5 and 6, the differences in the behaviour for differently-sized particles are evident in this flow. Fig. 10 shows another example of the *space-time* view for a continuous range of particle sizes in two different gravity environments.

Fig. 11 shows the *space-velocity* view for inertial particles seeded all across the domain. The visualizations show the influence of

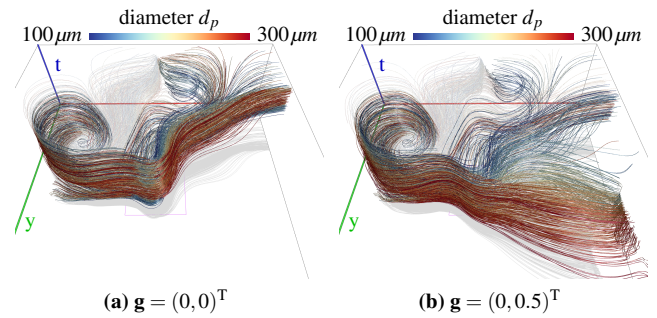


**Figure 10:** Inertial particle trajectories for different gravity vectors in the space-time view of the BORROMEAN data set. Adding gravity exerts a pull in a certain direction. In 10b, along the positive y-axis.

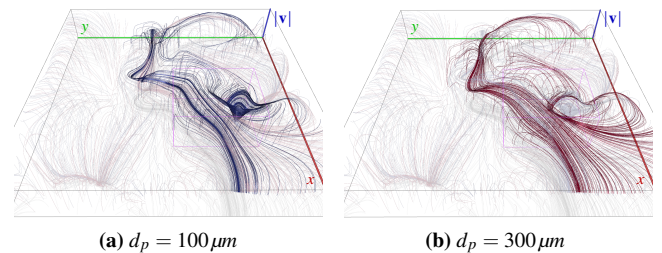


**Figure 11:** Space-velocity view on the BORROMEAN data set for zero initial velocity. A focus region is selected to point out the different flow behaviour in the vicinity of an attracting critical point.

attracting critical points on differently-sized inertial particles. The trajectories are brushed in the vicinity of the critical point. While light particles mostly follow the flow towards the critical point, heavy particles are carried outwards due to their own momentum and inertia. This behaviour is reflected in the type of the critical point [GG17], which may vary dependent on the particle size.

**Trefoil Knot.** Candelaresi and Brandenburg [CB11] provided the TREFOIL KNOT data set, which is another 3D magnetic field. This simulation contains three interlocked magnetic rings that decay over time. Same as Günther and Theisel [GT16a], we selected a 2D slice that shows swirling patterns. Fig. 12a gives an overview of the general flow motion in this data set. By subtly fading in the density volumes, the locations of the attracting critical points become visible as vertical structures. By releasing waves of differently-sized inertial particles at the same time with zero velocity, it becomes apparent that light particles approach the speed of the underlying flow faster and therefore travel farther distances in the same time. In Fig. 12b, a subset of the trajectories is selected and viewed in the *space-response* view to shed light onto the size-dependent differences. For the three released particle sizes, the differences are considerable due to the swirling motion that carries the inertial particles differently far outwards, which leads the lightest and heaviest particles into different parts of the domain. In Figs. 12c and 12d, the particles are released near one of the critical points with a different initial velocity. When releasing particles from rest ( $\mathbf{v}_0 = \mathbf{0}$ ), the swirling motion around a critical point becomes apparent. When varying the initial velocity in the range  $\alpha \in [-\pi/2, 0]$  and  $|\mathbf{v}| \in [0.67, 1]$  heavy particles are carried away from the critical point due to their inertia.

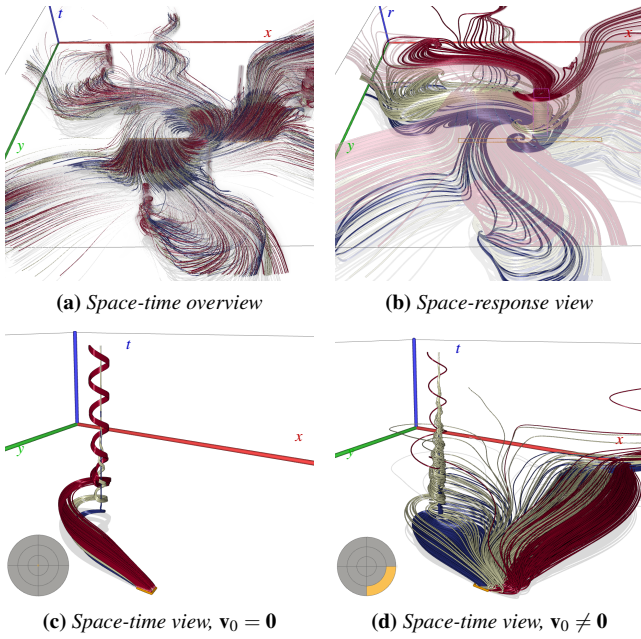


**Figure 12:** Study of swirling motion in the TREFOIL KNOT data set with differently-sized inertial particles and initial velocities. Here, for  $d_p = 100\mu\text{m}$  ( $\bullet$ ),  $d_p = 200\mu\text{m}$  ( $\circ$ ) and  $d_p = 300\mu\text{m}$  ( $\circ$ ).

## 5.2. Unsteady Flows

**Double Gyre.** The DOUBLE GYRE is a commonly used benchmark data sets for separating structures in unsteady 2D flows [SLM05]. In the context of inertial particles, Sudharsan et al. [SBR16] used it to study preferential particle settling, i.e., the size-dependent clustering after advection for a certain time. The time-periodic flow is defined in the domain  $D \times T = [0, 2] \times [0, 1] \times [0, 10]$  as

$$\mathbf{u}(x, y, t) = \begin{pmatrix} -0.1\pi \sin(f(x, t)\pi) \cos(y\pi) \\ 0.1\pi \cos(f(x, t)\pi) \sin(y\pi) \frac{d}{dx}f(x, t) \end{pmatrix} \quad (8)$$

with  $f(x, t) = a(t)x^2 + b(t)x$  and  $a(t) = 0.25 \sin(t\pi/5)$  and  $b(t) = 1 - 0.5 \sin(t\pi/5)$ .

Figs. 13a and 13b show the separation of inertial particles with different sizes for particles released both from rest ( $\mathbf{v}_0 = \mathbf{0}$ ) and with an initial velocity in the range  $\alpha \in [-\pi/2, 0]$  and  $|\mathbf{v}| \in [0.67, 1]$ . Particles are seeded in the left of the two counter-rotating vortices. When seeding from rest, most particles remain in the left vortex. However, when seeding with a velocity that pushes the particles towards the right vortex, the *space-time view* shows that heavy particles pass the separating material line of the underlying flow, leading the particles into the right half of the domain, whereas light particles quickly realign with the flow, keeping most of them in the left vortex. The difference in the trajectories is clearly visible without occlusions in the *space-response views* in Figs. 13c and 13d.

**Boussinesq Flow.** The BOUSSINESQ flow contains a convection simulation around a heated cylinder. The flow was simulated with Gerris Flow solver [Pop04] using the Boussinesq approximation. Since the motion in this flow is driven by the small heated cylinder, a fast jet stream occurs behind it. In Fig. 14, we released differently-

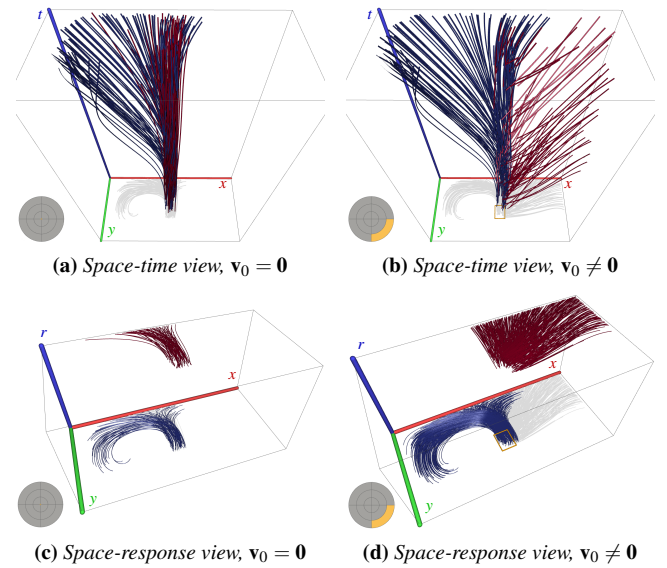


**Figure 13:** Coordinated views of the DOUBLE GYRE data set for different initial velocities, here  $d_p = 100\mu\text{m}$  ( $\bullet$ ) and  $d_p = 500\mu\text{m}$  ( $\circ$ ).

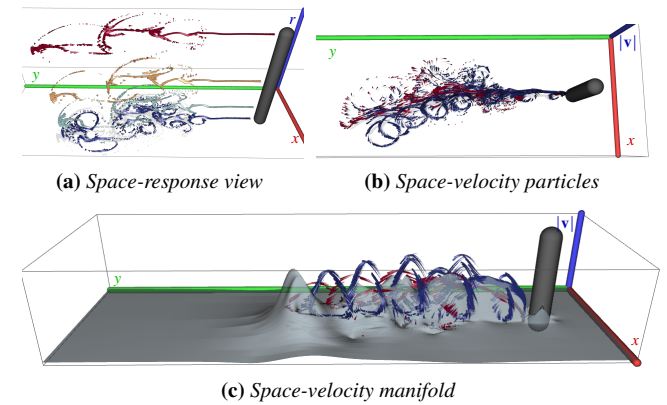


**Figure 14:** Trapping of inertial particles in the BOUSSINESQ flow. Here, for  $d_p = 40\mu\text{m}$  ( $\bullet$ ) and  $d_p = 300\mu\text{m}$  ( $\circ$ ).

sized inertial particles in the wake of the cylinder, i.e., directly in the jet core. Fig. 14a shows four different sizes of inertial particles in the *space-response view*. It can be seen very well that light particles follow the vortices, whereas heavy particles are less affected by such low-frequency flow features due to their inertia. In Fig. 14b, a particle animation is viewed from the top in the *space-velocity view*, which gives an impression of the rotating motion of light inertial particles. We refer to the accompanying video for an animation. Fig. 14c displays the attracting manifold of light particles, revealing an interesting behavior: Light particles are dragged during their rotating motion back into the jet core. This results in a periodic increase and decrease of the particle velocity, which is apparent in the space-velocity view. The attracting manifold shows the spatial regions in which particles accelerate. Heavy particles also accelerate in the jet, but they are carried outward into the slower regime.

**Cylinder Flow.** The CYLINDER flow was also simulated with Gerris Flow solver [Pop04] and contains a von-Kármán vortex street

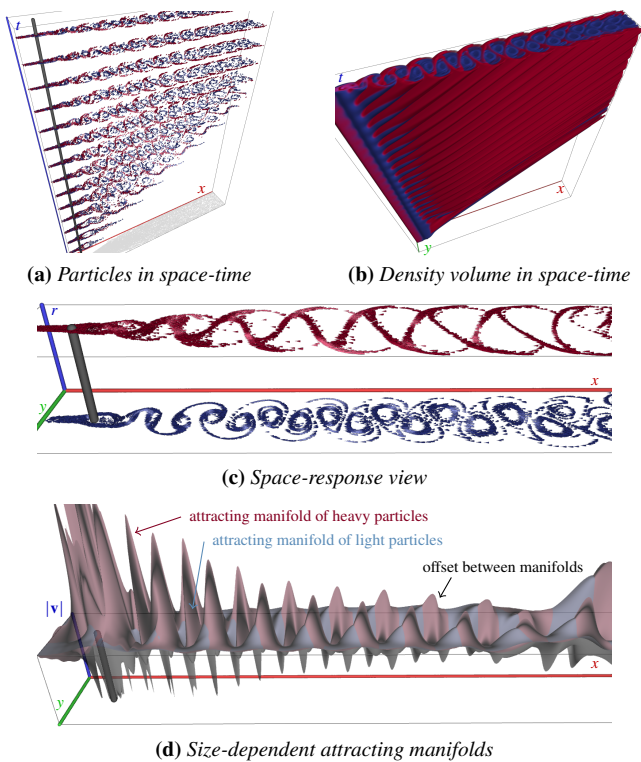


**Figure 15:** Inertial particles in the CYLINDER flow reveal the characteristic size-dependent preferential particle settling. Here with  $d_p = 40\ \mu\text{m}$  ( $\bullet$ ) and  $d_p = 300\ \mu\text{m}$  ( $\circ$ ).

in the wake of an obstacle. The viscous fluid with a Reynolds number of 160 was injected from the left into a channel bounded by solid walls with a slip boundary condition. Taking a look at the temporal evolution of particles in Fig. 15a reveals that light particles are trapped inside vortices, while heavy particles are pushed outward. This behaviour is also visible by the density volumes in Fig. 15b or the animated trajectories in the *space-response view* in Fig. 15c. These observations are consistent with previous studies and are an aspect of preferential particle settling [SBR16, GT17]. The two slowly attracting manifolds in Fig. 15d intersect and exhibit the symmetry of the vortices that drive the particle clustering. There is not only an inertia-dependent offset between manifolds, heavier particles also exhibit stronger variations and thus accelerations.

### 5.3. Performance

For all performance measurements, we used an Intel Core i7-4790K CPU with 4 GHz and 32 GB RAM, and an NVIDIA Quadro P6000 GPU. The image resolution was set to  $1300 \times 1000$  pixels. Table 1 reports a summary of the computation timings for each element of our three coordinated views for all data sets. We used a continuous range of particle sizes and thus one density volume. Shading was enabled for the rendering of the volumes and we disabled the animations in the trajectory views. Across all scenes, we obtained real-time frame rates. The volume rendering is currently the bottleneck.

For multiple discrete numbers of particle sizes, we compute the density for each size separately and store it in a two-component

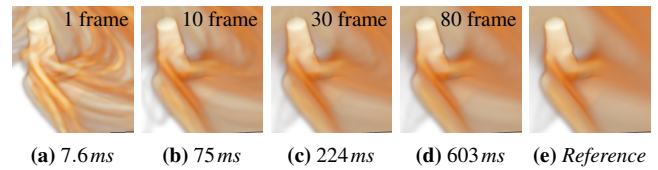


**Figure 16:** Close-up of the progressive computation of a density volume. The result converges quickly to the reference image.

texture (2 volumes) or a four-component texture (3 and 4 volumes). Note that three-component textures do not support hardware-accelerated texture filters, thus we fall back to four-component textures. The increasing rendering and computation time are shown in Table 2. Fig. 16 gives a close-up of the progressive density volume computation in the TREFOIL KNOT data set, showing that high quality results are reached after a few hundred milliseconds.

### 5.4. Parameters

By default, we use 1000 trajectories for both the static and the progressive line set. In the trajectory view, the choice is a matter of acceptable occlusion. In the progressive computation, it is a trade-off between performance and quality. With frameworks such as the one by Frey et al. [FSME14], the parameter could be selected automatically to adhere to a certain computation time budget. We select as resolution of the density volume the resolution of the underlying flow domain, which is in the order of 2–30 million voxels. The smoothing kernel during the density volume computation has a constant size of four voxels by default. A progressively shrinking kernel would yield sharper structures with vanishing bias [HJ09].

### 5.5. Discussion

**Limitations.** Rendering multiple size-dependent manifolds can lead to clutter in the *space-velocity view*. Thus, we show only one manifold for a user-specified size, and introduced ribbons. In this paper, we only focused on forward-integrated particles. A backward integration with source inversion approaches [GT16c, GT16b] would be interesting, though at the same time numerically and computationally more challenging. Currently, we support only up to four density volumes, as they are encoded in a single texture. For more than four density volumes, multiple textures could be used.

**Three-Dimensional Flows.** We used the third dimension to encode particle properties, namely time, velocity magnitude and response time. For 3D flows, other mapping strategies are required. The derivation of the slowly attracting manifold also holds in 3D, leading inertial particles in the limit to a certain velocity, cf. Eq. (4).

**Ensemble Visualization.** Inertial particles can be considered as a special case of ensembles, in which the ensemble members (the high-dimensional vector fields in which the particles live) are ordered by the response time. Obermaier and Joy [OJ14] classified ensemble visualizations into location-based and feature-based techniques. While the location-based methods display the vector variability [PWB\*09, JDKW15], feature-based techniques show the variation of derived properties such as isolines or tangent curves

Figure	Data set	Space-time view				Space-response view				Space-velocity view					
		T	V	I	S	T	V	I	S	T	V	I	S	M	R
4, 5, 6, 10	BORROMEAN	1.30	<b>9.5</b>	6.9	7.1	1.55	<b>9.5</b>	3.4	3.5	1.09	<b>11.6</b>	10.5	11.1	0.03	0.62
12	TREFOIL KNOT	1.65	<b>9.3</b>	6.2	6.7	2.10	<b>9.6</b>	6.5	6.9	1.40	<b>9.6</b>	6.2	6.5	0.04	1.90
8, 9	BENZENE	0.19	<b>5.3</b>	2.7	3.4	0.14	<b>5.5</b>	3.2	3.9	0.33	<b>5.5</b>	3.4	3.6	0.07	3.62
13	DOUBLE GYRE	0.34	<b>4.1</b>	2.3	2.4	0.14	<b>5.6</b>	3.6	3.9	0.18	<b>11.2</b>	6.9	7.3	0.04	3.41
14	BOUSSINESQ	1.38	<b>5.2</b>	4.6	4.9	0.35	<b>5.4</b>	4.8	5.1	1.12	<b>8.0</b>	6.5	7.0	0.40	0.65
15	CYLINDER	1.32	<b>6.1</b>	5.6	5.8	1.25	<b>6.0</b>	3.9	4.8	1.25	<b>9.1</b>	6.8	7.2	0.22	2.70

**Table 1:** Computation time in ms of trajectories ( $T$ ), density volumes ( $V$ ), isosurfaces ( $I$ ), isosurface slabs ( $S$ ), manifolds ( $M$ ), and ribbons ( $R$ ) in all views. The **bottleneck** is in all cases the computation of the density volumes, comprising trajectory tracing, voxelization, and rendering.

Num. volumes	Space-time	Space-response	Space-velocity
1	9.3	9.6	4.1
2	11.9	10.3	12.5
3 or 4	21.0	20.2	21.5

**Table 2:** Computation time (in ms) for different number of volumes and views in the TREFOIL KNOT data set. We use RGBA textures for both 3 and 4 volumes, since RGB textures do not support filtering.

[BFMW12, WMK13, MWK14, FBW16]. In the future, we focus on trajectory distributions from the perspective of ensemble visualization, as this augments the density plots with more information.

## 6. Conclusions

The motion of inertial particles is a high-dimensional problem, as it involves position, velocity, time and particle size. In this paper, we proposed a novel method to visualize the phase space of inertial particles under all possible seeding configurations. Our three coordinated views allow the user to explore the domains interactively and to release particles of different sizes and with different initial conditions. Each view studies different aspects, such as the temporal evolution, the size-dependent behaviour and the interaction with the slow attracting manifold. The first view is dedicated to the temporal evolution, providing detailed observations of individual trajectories and abstraction through the progressive computation of density volumes that are viewed with direct volume rendering and isosurfaces. The second view provides a clear separation by the particle size, which greatly helps to explore the size-dependent differences in heterogeneous mixtures of particles. The last view places the trajectories in a space-velocity domain and shows the attracting manifold as context. Since the manifold is particle size-dependent, we provide ribbons that show the deviation from the manifold locally for each particle. In the future, we would like to study other equations of motion, as well as two-way coupled inertial particle systems, in which the underlying flow itself is influenced by the particles.

## Appendix A: Slow Attracting Manifold

In the following, we derive the slow attracting manifold. The derivation closely follows the more general version of Haller and Sapsis [HS08]. To study the manifold, we first rewrite the equation of motion from Eq. (1). For this, we introduce the small parameter  $\varepsilon = r \ll 1$ , which is used to scale the time  $\phi = t_0 + \varepsilon\tau$  of the ODE:

$$\frac{d}{d\tau} \begin{pmatrix} \mathbf{x} \\ \mathbf{v} \\ \phi \end{pmatrix} = \begin{pmatrix} \varepsilon \mathbf{v} \\ \mathbf{u}(\mathbf{x}, \phi) - \mathbf{v} + \varepsilon \mathbf{g} \\ \varepsilon \end{pmatrix} \quad (9)$$

In Eq. (9), we see that  $\mathbf{x}$  now changes slowly (scaled with  $\varepsilon$ ), whereas  $\mathbf{v}$  changes fast. This rescaling is common in singular perturbation theory and serves two purposes: First, it implicitly scales down the step size  $\frac{d\phi}{d\tau} = \varepsilon$  for small particles, since in Eq. (1) the  $\mathbf{v}$  component would otherwise go towards infinite speed for  $r \ll 1$ . Second, it completely removes any division by  $\varepsilon$ .

Fenichel [Fen79] showed that autonomous ODEs of the form in Eq. (9) contain attracting manifolds  $M_\varepsilon$  that depend on  $\varepsilon$  and that their velocity  $\mathbf{w}(\mathbf{x}, \phi)$  can be described by a Taylor expansion:

$$M_\varepsilon = \{(\mathbf{x}, \mathbf{w}, \phi) : \mathbf{w}(\mathbf{x}, \phi), (\mathbf{x}, \phi) \in D \times T\} \quad (10)$$

$$\mathbf{w}(\mathbf{x}, \phi) = \mathbf{u}(\mathbf{x}, \phi) + \sum_{i=1}^k \varepsilon^i \mathbf{u}^i(\mathbf{x}, \phi) + O(\varepsilon^{k+1}) \quad (11)$$

where  $\mathbf{u}^i$  are yet unknown vector fields. Eq. (11) contains the velocity in the manifold, which we differentiate to get the acceleration:

$$\begin{aligned} \frac{d\mathbf{w}}{d\tau} &= \frac{d\mathbf{u}}{d\mathbf{x}} \frac{d\mathbf{x}}{d\tau} + \frac{d\mathbf{u}}{d\phi} \frac{d\phi}{d\tau} + \sum_{i=1}^k \varepsilon^i \left[ \frac{d\mathbf{u}^i}{d\mathbf{x}} \frac{d\mathbf{x}}{d\tau} + \frac{d\mathbf{u}^i}{d\phi} \frac{d\phi}{d\tau} \right] + O(\varepsilon^{k+1}) \\ &= \varepsilon \frac{D\mathbf{u}}{D\tau} + \sum_{i=1}^k \varepsilon^{i+1} \frac{D\mathbf{u}^i}{D\tau} + O(\varepsilon^{k+1}) \end{aligned} \quad (12)$$

with the velocity of the underlying flow  $\frac{d\mathbf{x}}{d\tau} = \varepsilon \mathbf{u}(\mathbf{x}, t)$  and recalling  $\frac{d\phi}{d\tau} = \varepsilon$ . Eq. (9) gives us the acceleration of an inertial particle, and Eq. (12) is the acceleration of the attracting manifold. The two are equal when the inertial particle reaches the manifold. The acceleration of the inertial particle on the manifold is found by inserting Eq. (11) as  $\mathbf{v}$  into the velocity component of Eq. (9):

$$\frac{d\mathbf{v}}{d\tau}|_{M_\varepsilon} = \varepsilon \mathbf{g} - \sum_{i=1}^k \varepsilon^i \mathbf{u}^i + O(\varepsilon^{k+1}) \quad (13)$$

By setting  $\frac{d\mathbf{v}}{d\tau}|_{M_\varepsilon} = \frac{d\mathbf{w}}{d\tau}$  using Eqs. (12) and (13) we obtain:

$$\varepsilon \mathbf{g} - \sum_{i=1}^k \varepsilon^i \mathbf{u}^i = \varepsilon \frac{D\mathbf{u}}{D\tau} + \sum_{i=2}^{k+1} \varepsilon^i \frac{D\mathbf{u}^{i-1}}{D\tau} \quad (14)$$

Solving for  $\mathbf{u}^i$  by comparing terms with equal powers of  $\varepsilon$  in Eq. (14) and passing back to the original time  $t$ , we determine the  $\mathbf{u}^i$  that define the attracting manifold, with  $k > 1$ :

$$\mathbf{u}^1(\mathbf{x}, t) = \mathbf{g} - \frac{D\mathbf{u}(\mathbf{x}, t)}{Dt}, \quad \mathbf{u}^k(\mathbf{x}, t) = -\frac{D\mathbf{u}^{k-1}(\mathbf{x}, t)}{Dt} \quad (15)$$

By inserting Eq. (15) into Eq. (11), a first-order approximation of the asymptotic inertial particle motion on the slow manifold is:

$$\mathbf{w}(\mathbf{x}, t) = \mathbf{u}(\mathbf{x}, t) + \varepsilon \mathbf{u}^1(\mathbf{x}, t) = \mathbf{u}(\mathbf{x}, t) + \varepsilon \left[ \mathbf{g} - \frac{D\mathbf{u}(\mathbf{x}, t)}{Dt} \right] \quad (16)$$

## References

- [BBC\*11] BEC J., BIFERALE L., CENCINI M., LANOTTE A. S., TOSCHI F.: Spatial and velocity statistics of inertial particles in turbulent flows. *Journal of Physics: Conference Series* 333, 1 (2011), 012003. 2, 3
- [BFMW12] BÜRGER K., FRAEDRICH R., MERHOF D., WESTERMANN R.: Instant visitation maps for interactive visualization of uncertain particle trajectories. In *Proc. SPIE 8294, Visualization and Data Analysis* (2012), SPIE, p. 82940P. 10
- [CB11] CANDELAESI S., BRANDENBURG A.: Decay of helical and nonhelical magnetic knots. *Phys. Rev. E* 84 (2011), 016406. 7
- [CGP\*10] CASCIOLA C. M., GUALTIERI P., PICANO F., SARDINA G., TROIANI G.: Dynamics of inertial particles in free jets. *Physica Scripta* 2010, T142 (2010), 014001. 2
- [CST98] CROWE C., SOMMERFIELD M., TSUJI Y.: *Multiphase Flows with Droplets and Particles*. CRC Press, 1998. 2
- [FBW16] FERSTL F., BÜRGER K., WESTERMANN R.: Streamline variability plots for characterizing the uncertainty in vector field ensembles. *IEEE Transactions on Visualization and Computer Graphics (Proc. IEEE Scientific Visualization 2015)* 22, 1 (2016), 767–776. 4, 6, 10
- [Fen79] FENICHEL N.: Geometric singular perturbation theory for ordinary differential equations. *Journal of Differential Equations* 31, 1 (1979), 53–98. 10
- [FH15] FARAZMAND M., HALLER G.: The Maxey–Riley equation: Existence, uniqueness and regularity of solutions. *Nonlinear Analysis: Real World Applications* 22 (2015), 98–106. 2
- [FSME14] FREY S., SADLO F., MA K.-L., ERTL T.: Interactive progressive visualization with space-time error control. *IEEE Transactions on Visualization and Computer Graphics* 20, 12 (2014), 2397–2406. 9
- [GG17] GÜNTHER T., GROSS M.: Flow-induced inertial steady vector field topology. *Computer Graphics Forum (Proc. Eurographics)* 36, 2 (2017), 143–152. 2, 3, 7
- [GKKT13] GÜNTHER T., KUHN A., KUTZ B., THEISEL H.: Mass-dependent integral curves in unsteady vector fields. *Computer Graphics Forum (Proc. EuroVis)* 32, 3 (2013), 211–220. 2, 3
- [GPPMn15] GARABOA-PAZ D., PÉREZ-MUÑUZURI V.: A method to calculate finite-time Lyapunov exponents for inertial particles in incompressible flows. *Nonlin. Proc. in Geophys.* 22, 5 (2015), 571–577. 3
- [GT14] GÜNTHER T., THEISEL H.: Vortex cores of inertial particles. *IEEE Transactions on Visualization and Computer Graphics (Proc. IEEE SciVis)* 20, 12 (2014), 2535–2544. 2, 3
- [GT15] GÜNTHER T., THEISEL H.: Finite-time mass separation for comparative visualizations of inertial particles. *Computer Graphics Forum (Proc. EuroVis)* 34, 3 (2015), 471–480. 2, 3
- [GT16a] GÜNTHER T., THEISEL H.: Inertial steady 2D vector field topology. *Computer Graphics Forum (Proc. Eurographics)* 35, 2 (2016), 455–466. 2, 3, 7
- [GT16b] GÜNTHER T., THEISEL H.: Singularities of the inertial flow map gradient. *Proc. Vision, Modeling, and Visualization (VMV)* (2016), 69–76. 3, 9
- [GT16c] GÜNTHER T., THEISEL H.: Source inversion by forward integration in inertial flows. *Computer Graphics Forum (Proc. EuroVis)* 35, 3 (2016), 371–380. 2, 3, 9
- [GT17] GÜNTHER T., THEISEL H.: Backward finite-time Lyapunov exponents in inertial flows. *IEEE Transactions on Visualization and Computer Graphics (Proc. IEEE SciVis 2016)* 23, 1 (2017), 970–979. 2, 3, 9
- [GTG17] GÜNTHER T., THEISEL H., GROSS M.: Decoupled opacity optimization for points, lines and surfaces. *Computer Graphics Forum (Proc. Eurographics)* 36, 2 (2017), 153–162. 4
- [HJ09] HACHISUKA T., JENSEN H. W.: Stochastic progressive photon mapping. *ACM Transaction on Graphics (Proc. SIGGRAPH Asia)* 28, 5 (2009), 141:1–141:8. 6, 9
- [HLSR09] HADWIGER M., LJUNG P., SALAMA C. R., ROPINSKI T.: Advanced illumination techniques for GPU-based volume raycasting. In *ACM SIGGRAPH 2009 Courses* (New York, NY, USA, 2009), SIGGRAPH '09, ACM, pp. 2:1–2:166. 6
- [HS08] HALLER G., SAPSIS T.: Where do inertial particles go in fluid flows? *Physica D: Nonlinear Phenomena* 237 (May 2008), 573–583. 2, 3, 7, 10
- [HY00] HALLER G., YUAN G.: Lagrangian coherent structures and mixing in two-dimensional turbulence. *Physica D: Nonlinear Phenomena* 147, 3–4 (2000), 352–370. 3
- [JDKW15] JAREMA M., DEMIR I., KEHRER J., WESTERMANN R.: Comparative visual analysis of vector field ensembles. In *IEEE Conference on Visual Analytics Science and Technology (VAST)* (Oct 2015), pp. 81–88. 9
- [Kei02] KEIM D. A.: Information visualization and visual data mining. *IEEE Transactions on Visualization and Computer Graphics* 8, 1 (Jan 2002), 1–8. 4
- [KGRK14] KUTZ B. M., GÜNTHER T., RUMPF A., KUHN A.: Numerical examination of a model rotor in brownout conditions. In *Proceedings of the American Helicopter Society* (2014), no. AHS2014-000343. 2
- [MGvW98] MULDER J. D., GROEN F. C. A., VAN WIJK J. J.: Pixel masks for screen-door transparency. In *Visualization '98. Proceedings* (Oct 1998), pp. 351–358. 6
- [MLP\*10] MCLOUGHLIN T., LARAMEE R. S., PEIKERT R., POST F. H., CHEN M.: Over two decades of integration-based, geometric flow visualization. *Computer Graphics Forum* 29, 6 (2010), 1807–1829. 1
- [MR83] MAXEY M. R., RILEY J. J.: Equation of motion for a small rigid sphere in a nonuniform flow. *Physics of Fluids* 26, 4 (1983), 883–889. 2
- [MWK14] MIRZARGAR M., WHITAKER R. T., KIRBY R. M.: Curve boxplot: Generalization of boxplot for ensembles of curves. *IEEE Transactions on Visualization and Computer Graphics* 20, 12 (Dec 2014), 2654–2663. 10
- [OJ14] OBERMAIER H., JOY K. I.: Future challenges for ensemble visualization. *IEEE Computer Graphics and Applications* 34, 3 (May 2014), 8–11. 9
- [PD09] PENG J., DABIRI J. O.: Transport of inertial particles by Lagrangian coherent structures: Application to predator–prey interaction in jellyfish feeding. *Journal of Fluid Mechanics* 623 (3 2009), 75–84. 2, 3
- [Pop04] POPINET S.: Free computational fluid dynamics. *Cluster World* 2, 6 (2004). 8
- [PSGC11] PICANO F., SARDINA G., GUALTIERI P., CASCIOLA C.: DNS of a free turbulent jet laden with small inertial particles. In *Direct and Large-Eddy Simulation VIII*, Kuerten H., Geurts B., Armenio V., Fröhlich J., (Eds.), vol. 15 of *ERCOFTAC Series*. Springer Netherlands, 2011, pp. 189–194. 2
- [PTVF96] PRESS W. H., TEUKOLSKY S. A., VETTERLING W. T., FLANNERY B. P.: *Numerical recipes in C*, vol. 2. Cambridge university press Cambridge, 1996. 6
- [PWB\*09] POTTER K., WILSON A., BREMER P. T., WILLIAMS D., DOUTRIAUX C., PASCUCCI V., JOHNSON C. R.: Ensemble-vis: A framework for the statistical visualization of ensemble data. In *IEEE International Conference on Data Mining Workshops* (Dec 2009), pp. 233–240. 9
- [RSBE01] ROETTGER S., SCHULZ M., BARTELHEIMER W., ERTL T.: Automotive soiling simulation based on massive particle tracing. In *Data Visualization 2001*, Eurographics. Springer Vienna, 2001, pp. 309–317. 2, 3
- [SBHH15] SHORT C. R., BLAZEWSKI D., HOWELL K. C., HALLER G.: Stretching in phase space and applications in general nonautonomous multi-body problems. *Celestial Mechanics and Dynamical Astronomy* 122 (2015), 213–238. 3
- [SBL11] SYDNEY A., BAHARANI A., LEISHMAN J. G.: Understanding brownout using near-wall dual-phase flow measurements. In *Proceedings*

- of the American Helicopter Society (Virginia Beach, VA, May 2011), 67th Annual Forum. 2
- [SBR16] SUDHARSAN M., BRUNTON S. L., RILEY J. J.: Lagrangian coherent structures and inertial particle dynamics. *Phys. Rev. E* 93 (Mar 2016), 033108. 3, 7, 8, 9
- [SGL10] SYAL M., GOVINDARAJAN B., LEISHMAN J. G.: Mesoscale sediment tracking methodology to analyze brownout cloud developments. In *Proceedings of the American Helicopter Society, 66th Annual Forum* (2010). 2
- [SH09] SAPSIS T. P., HALLER G.: Inertial particle dynamics in a hurricane. *Journal of the Atmospheric Sciences* 66, 8 (2009), 2481–2492. 3
- [Sha05] SHADDEN S. C.: Lagrangian coherent structures. <http://mmae.iit.edu/shadden/LCS-tutorial/>, 2005. 3
- [SHT11] SHORT C., HOWELL K., TRICOCHÉ X.: Lagrangian coherent structures in the restricted three-body problem. In *Proc. AAS/AIAA Space Flight Mechanics Meeting* (2011), pp. 11–250. 2
- [SJJ\*17] SAGRISTÀ A., JORDAN S., JUST A., DIAS F., NONATO L. G., SADLO F.: Topological analysis of inertial dynamics. *IEEE Transactions on Visualization and Computer Graphics (Proc. IEEE SciVis 2016)* 23, 1 (2017), 950–959. 2, 3
- [SL99] SHAO Y., LI A.: Numerical modelling of saltation in the atmospheric surface layer. *Boundary-Layer Meteor.* 91 (1999), 199–225. 2
- [SLM05] SHADDEN S. C., LEKIEN F., MARSDEN J. E.: Definition and properties of Lagrangian coherent structures from finite-time Lyapunov exponents in two-dimensional aperiodic flows. *Physica D: Nonlinear Phenomena* 212, 3–4 (2005), 271–304. 8
- [SPH11] SAPSIS T., PENG J., HALLER G.: Instabilities on prey dynamics in jellyfish feeding. *Bull Math Biol.* 73, 8 (2011), 1841–1856. 2
- [WLG97] WEGENKITTL R., LÖFFELMANN H., GRÖLLER E.: Visualizing the behaviour of higher dimensional dynamical systems. In *Proc. Visualization '97* (1997), IEEE, pp. 119–125. 3
- [WMK13] WHITAKER R. T., MIRZARGAR M., KIRBY R. M.: Contour boxplots: A method for characterizing uncertainty in feature sets from simulation ensembles. *IEEE Transactions on Visualization and Computer Graphics* 19, 12 (Dec 2013), 2713–2722. 10
- [ZSH96] ZÖCKLER M., STALLING D., HEGE H.-C.: Interactive visualization of 3D vector fields using illuminated stream lines. In *IEEE Visualization* (1996), pp. 107–113. 4, 7